Gain- and Loss-Induced Topological Insulating Phase in a Non-Hermitian Electrical Circuit

Shuo Liu,[1,2] Shaojie Ma,[1,2] Cheng Yang,[3] Lei Zhang,[3] Wenlong Gao,[1] Yuan Jiang Xiang,[1,*] Tie Jun Cui,[3,†] and Shuang Zhang[2,‡]

[1] *International Collaborative Laboratory of 2D Materials for Optoelectronic Science & Technology of Ministry of Education, Institute of Microscale Optoelectronics (IMO), Shenzhen University, Shenzhen 518060, China*

[2] *School of Physics and Astronomy, University of Birmingham, Birmingham B15 2TT, United Kingdom*

[3] *State Key Laboratory of Millimeter Waves, Southeast University, Nanjing 210096, China*

(Received 1 July 2019; revised manuscript received 20 November 2019; published 24 January 2020)

There have been considerable efforts devoted to the study of topological phases in certain non-Hermitian systems that possess real eigenfrequencies in the presence of gain and loss. However, it is challenging to experimentally realize such non-Hermitian topological insulators in either quantum or photonic systems, due to difficulties in introducing controlled gain and loss. On the other hand, the wide choices of active circuit components provide us with unprecedented convenience and flexibility in engineering non-Hermitian topological insulators in electrical circuits. Here, we report on the experimental realization of a one-dimensional non-Hermitian topological circuit that exhibits topologically protected edge states purely induced by gain and loss. We show that, by tuning the value of the positive and negative resistors in the circuit, our system can switch between different topological phase regions. The topological edge states and interface states are observed at the circuit edge and at the interface between a trivial and nontrivial circuit; these states are manifested by a prominent impedance peak at the midgap frequency, which is topologically robust to variations of circuit parameters. Our work opens up an alternative gateway towards actively controllable topological systems.

DOI: 10.1103/PhysRevApplied.13.014047

I. INTRODUCTION

Topological physics is concerned with the study of quantized parameters that are invariant under continuous variations of the system. Originating from condensed matter physics, investigations into topological phenomena are extended to classical systems, such as photonics, acoustics, and mechanics. In particular, nontrivial topology in classical systems has great potential in applications such as lasers [1,2] and manipulation of acoustic [3,4] and mechanical waves [5,6]. Recently, electrical circuits are emerging as a powerful platform for exploring topological physics, allowing the demonstration of some topological phenomena, such as the spin Hall effect [7,8], Haldane model, magnetic dipole [9], topologically protected edge state in the one-dimensional (1D) Su–Schrieffer–Heeger (SSH) model [10,11], Weyl state, and the Fermi-arc surface state in three-dimensional (3D) [12–14] and higher-order topological states in electrical circuits [15–17]. It is also more convenient to add a strong nonlinear effect to topological circuits than to photonic and quantum systems. By replacing the coupling capacitor in a 1D SSH circuit chain with two back-to-back varactor diodes, self-induced topological transitions, as a function of the input intensity, are realized [18]. More interestingly, the operational amplifier (OA) is introduced to a circuit as a gain element to realize a non-Hermitian topological band gap that is fully reconfigurable via tuning the value of resistors [19] and to observe a bulk Fermi-arc state (bulk drumhead states) that connects the exceptional points (exceptional lines) [20].

Non-Hermitian systems have attracted much attention since the introduction of the concept of parity-time (PT) reflection symmetry by Bender and Boettcher in 1998 [21]. A non-Hermitian system may experience a phase transition at an exceptional point (EP) in the wave momentum, where the eigenfrequencies change from real to complex numbers. In such non-Hermitian systems, complex potential profiles, representing balanced gain and loss, are critical factors for achieving real eigenvalues. Due to the difficulty of generating gain and loss in quantum systems, considerable efforts are made for the study of PT symmetry in photonic systems [22–25]. The combination of PT symmetry and topological physics leads to interesting physics that do not exist in Hermitian systems [26–28]. In particular,

*yjxiang@szu.edu.cn
†Tjcui@seu.edu.cn
‡zhang@bham.ac.uk

it was recently discovered by Takata and Notomi that a topological insulating state could be achieved solely by adding static gain and loss to a topologically trivial structure [29]. They demonstrated theoretically a 1D photonic lattice with a topological insulating phase being controlled by the gain and loss profiles, and they showed that the topological edge mode could exist at the boundary of a finite lattice, or the interface between a trivial and a nontrivial lattice, due to particle-hole symmetry [30] or the pseudo-anti-Hermiticity. However, such gain- and loss-induced topological systems are not experimentally observed.

Here, we present the design and experimental realization of a non-Hermitian electrical circuit, the nontrivial topology of which solely arises from the introduction of gain and loss. The circuit exhibits four different phase regions at different combinations of the gain and loss settings, three of which support a topological edge state in a nontrivial midgap opened by the balanced positive and negative resistance. For convenient experimental observation of the edge-interface state from the impedance spectra, a global-loss offset is introduced to our circuit to shift the midgap edge mode to a purely real eigenvalue. Circuit simulations and experiments are carried out to confirm the existence of gain- and loss-induced topological edge states localized at the end of a 10-unit-cell circuit chain.

II. CIRCUIT DIAGRAM AND ITS CHARACTERIZATION

Here, we consider a 1D non-Hermitian resonator array, where the topological phases are solely controlled by gain and loss $\pm g_1$ and $\pm g_2$ elaborately arranged in a pair of resonator dimers, as sketched in Fig. 1(a). Gain and loss can be conveniently introduced into electrical circuits in many ways, for example, by employing negative and positive resistors, which enable a direct mapping of the theoretical model presented in Fig. 1(a) to the electrical circuit, as illustrated in Fig. 1(b). Each resonant circuit is composed of an inductor, L, and a capacitor, C, connected in parallel, working as a parallel LC resonant tank. Resistors R_a, R_b and negative resistors $-R_a$, $-R_b$ are added to the corresponding resonant circuits as loss and gain modules, respectively. An additional resistor, R_c, is added to each resonant circuit as a global-loss offset to shift the imaginary part of the eigenfrequency of the edge state to zero, which results in a maximum resonant impedance peak at the edge state. All four resonant circuits are grounded at one end, while the other end is connected to their adjacent ones through two coupling capacitors, C. Figure 1(c) shows the print circuit board (PCB) layout of one circuit unit cell. The non-Hermitian topological circuit is thus constructed by a periodic arrangement of the unit cell in Fig. 1(b).

One of the key elements for realizing the gain- and loss-induced non-Hermitian circuit is the negative resistor, which functions as a power source that pumps energy into the circuit. The negative resistor module, also known as the negative impedance converter with current inversion (INIC), consists of an OA accompanied by a negative feedback network, as sketched in Fig. 1(d). The virtual open- and short-circuit conditions between the inverting input and noninverting input pins of the OA force the input current, I_{in} (with magnitude of V_0/R_c) out of phase with respect to the voltage, V_0, applied to it. This implies that the current in a negative resistor flows from low electrical potential to high electrical potential, which is opposite to

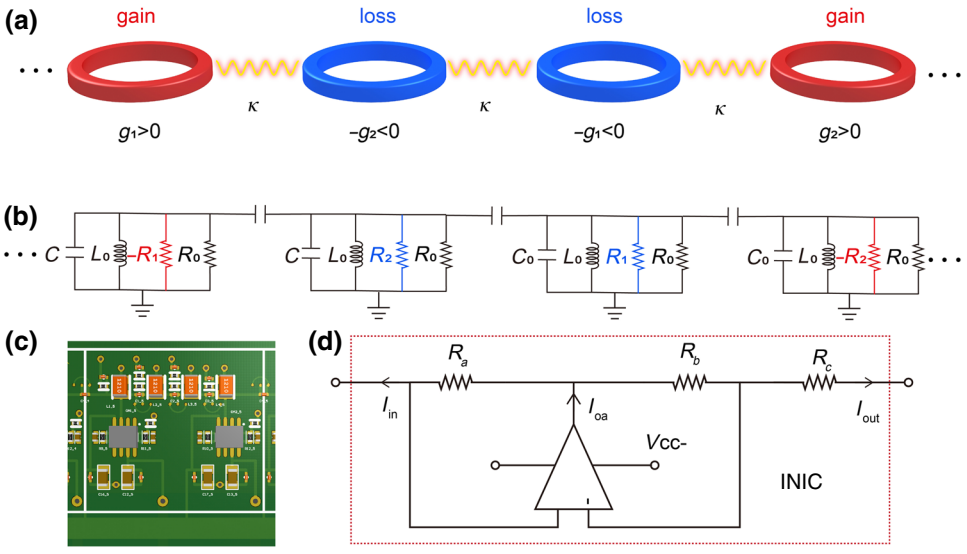

FIG. 1. Schematic and circuit diagram of the gain- and-loss induced non-Hermitian circuit. (a) Schematic of a single cell of the gain- and loss-induced non-Hermitian model in the quantum system. (b) Unit cell of the circuit implementation. (c) PCB layout of one unit cell of the non-Hermitian circuit. (d) Circuit schematic of the negative resistor module.

that of a positive (normal) resistor. This counterintuitive behavior of the negative resistor makes it consume negative energy from, or pumps positive energy into, the circuit, with an amount of electrical energy of $P = {V_0}^2/R_c$, which is exactly the same as that being consumed on a positive resistor, R_0.

A circuit with time-dependent $e^{i\omega}$ can be described by the following equation, which links the total input current, I_a, flowing out of node a and voltage V_b across nodes a and b,

$$I_a = \sum_b \left[i\omega C_{ab}(\omega) + \sigma_{ab} + \frac{1}{i\omega} W_{ab}(\omega) \right] V_b = J_{ab}(\omega) V_b, \tag{1}$$

and its matrix form, $\mathbf{I} = (i\omega\mathbf{C} + \boldsymbol{\sigma} + 1/i\omega\mathbf{W})V = \mathbf{J}(\omega)\mathbf{V}$, where $\mathbf{J}(\omega)$ is the circuit Laplacian, which contains the complete information of a circuit. $\mathbf{C}$, $\mathbf{W}$, and $\boldsymbol{\sigma}$ are the Laplacian matrices of capacitance, inverse inductance, and conductance, respectively. The diagonal and off-diagonal components represent the self-admittance of a certain node and the mutual admittance between two nodes, respectively. For our circuit, $\mathbf{J}(\omega)$ is a complex matrix, as it involves resistive terms. The bulk-circuit Laplacian $\mathbf{J}(\omega,q)$ in the momentum space can be written into a 4×4 matrix by considering the unit-cell circuit in the periodic boundary condition [Fig. 1(b)],

$$\begin{aligned}\mathbf{J}(\omega,q) &= i\omega\mathbf{C} + \boldsymbol{\sigma} + \frac{1}{i\omega}\mathbf{W} \\ &= i\omega \begin{bmatrix} 2C + C_0 + \frac{\sigma_1+\sigma_0}{i\omega} - \frac{1}{\omega^2 L_0} & -C & 0 & -Ce^{-iq} \\ -C & 2C + C_0 - \frac{\sigma_2-\sigma_0}{i\omega} - \frac{1}{\omega^2 L_0} & -C & 0 \\ 0 & -C & 2C + C_0 - \frac{\sigma_1-\sigma_0}{i\omega} - \frac{1}{\omega^2 L_0} & -C \\ -Ce^{iq} & 0 & -C & 2C + C_0 + \frac{\sigma_2+\sigma_0}{i\omega} - \frac{1}{\omega^2 L_0} \end{bmatrix},\end{aligned} \tag{2}$$

where q is the Bloch wave number linking a certain unit cell with its neighboring unit cells through $V_{n\pm1}(t) = V_n(t)e^{\pm iq}$. Although the circuit Laplacian in Eq. (2) does not give directly the eigenfrequency of the circuit, as it itself is frequency dependent, it can be used to analyze the topological invariant and symmetries of a topological circuit. The inductive and capacitive components in the diagonal terms are cancelled out at $\omega = \omega_0 = 1/\sqrt{3C_0L_0}$,

$$\mathbf{J}(\omega_0,q) = \begin{bmatrix} \sigma_1 & -i\omega_0 C & 0 & -i\omega_0 Ce^{-iq} \\ -i\omega_0 C & -\sigma_2 & -i\omega_0 C & 0 \\ 0 & -i\omega_0 C & -\sigma_1 & -i\omega_0 C \\ -i\omega_0 Ce^{iq} & 0 & -i\omega_0 C & \sigma_2 \end{bmatrix}. \tag{3}$$

Without global loss offset σ_0, the circuit Laplacian $J(\omega_0,q)$ preserves a pseudo-Hermiticity $S^{-1}(q)J(\omega_0,q)S(q) = J^\dagger(\omega_0,q)$, in which $S^{-1}(q) = S(q) = \hat{\sigma}_x \otimes [\cos(k/2)]\hat{I}_2 + \hat{\sigma}_y \otimes [\sin(k/2)]\hat{I}_2$ represents a half-period translation, $\hat{\sigma}_{x,y,z}$ are the Pauli matrices, and $\hat{I}_2$ is the 2×2 identity matrix. It also features a pseudo-anti-Hermiticity $J(\omega_0,q) = -\hat{\eta}J^\dagger(\omega_0,q)\hat{\eta}$, where $\hat{\eta} = \hat{I}_2 \otimes \hat{\sigma}_z = \mathrm{diag}(1,-1,1,-1)$ [31,32]. Such a symmetry is known to induce the nontrivial topology-forcing pairwise eigenvalues $j(\omega_0,q)$ $= -j^*(\omega_0,q)$. Notably, these symmetries are similar to those in quantum systems [29] due to their similarity in structural configuration.

A new topological invariant, the normalized Berry phase $W = \sum_s (i/2\pi)\left((1/2)\int_{-2\pi}^{2\pi} dq \langle\langle \psi_{B,s}|\psi_{B,s}\rangle\right)$ [29,33], is introduced to determine the topology of the circuit under different gain and loss configurations, which is obtained by first calculating the inner product of the right and left eigenvectors in a 4π period in the momentum space and then summing over all bands. Here, $|\psi'_{B,s}\rangle$ and $|\psi'_{B,s}\rangle\rangle$ are the right eigenvectors and corresponding left eigenvectors of $J(\omega_0,q)$, and they should be normalized as $\langle\langle\psi'_{B,s}|\partial_q|\psi'_{B,s}\rangle\rangle \big/ \langle\langle\psi'_{B,s}|\psi'_{B,s}\rangle\rangle$ before being sent for the calculation of W [34]. In contrast to the original definition of the Berry phase for the 1D model, which is calculated within one loop of the first Brillouin zone, here the loop spans two rounds of the first Brillouin zone. It is calculated that W equals one for $\sigma_1\sigma_2 > 0$, indicating a topologically nontrivial state, but becomes zero for $\sigma_1\sigma_2 < 0$, indicating a trivial state.

To obtain the eigenfrequency of the circuit, we further construct the Hamiltonian from the circuit Laplacian matrix $\mathbf{C}$, $\mathbf{W}$, $\boldsymbol{\sigma}$ (see Note S2 and Eqs. (S7)–(S9) within the Supplemental Material [35] in the new basis of $\psi(t) =$

$[V(t), \dot{V}(t)]$),

$$H = i\begin{bmatrix} \frac{\sigma}{C} & \frac{W}{C} \\ -I & 0 \end{bmatrix}. \quad (4)$$

It is proved that the topological invariant of the circuit calculated from both the circuit Laplacian and circuit Hamiltonian are identical [19]. As explained in Note S2 within the Supplemental Material [35], the circuit Laplacian and circuit Hamiltonian are connected in a way that the zeros of the eigenvalue spectra of the circuit Laplacian correspond to the eigenvalues of the circuit Hamiltonian (i.e., eigenfrequencies of the circuit) [13,15,19].

III. BULK PROPERTIES AT DIFFERENT PHASES

To analyze how the band structure evolves among different phases at different gain and loss settings (σ_1, σ_2) under a fixed global-loss offset of $\sigma_0 = 2.1$ mS, in Fig. 2(a) we plot the phase diagram of the bulk circuit model, which is numerically obtained by analyzing the band structure at

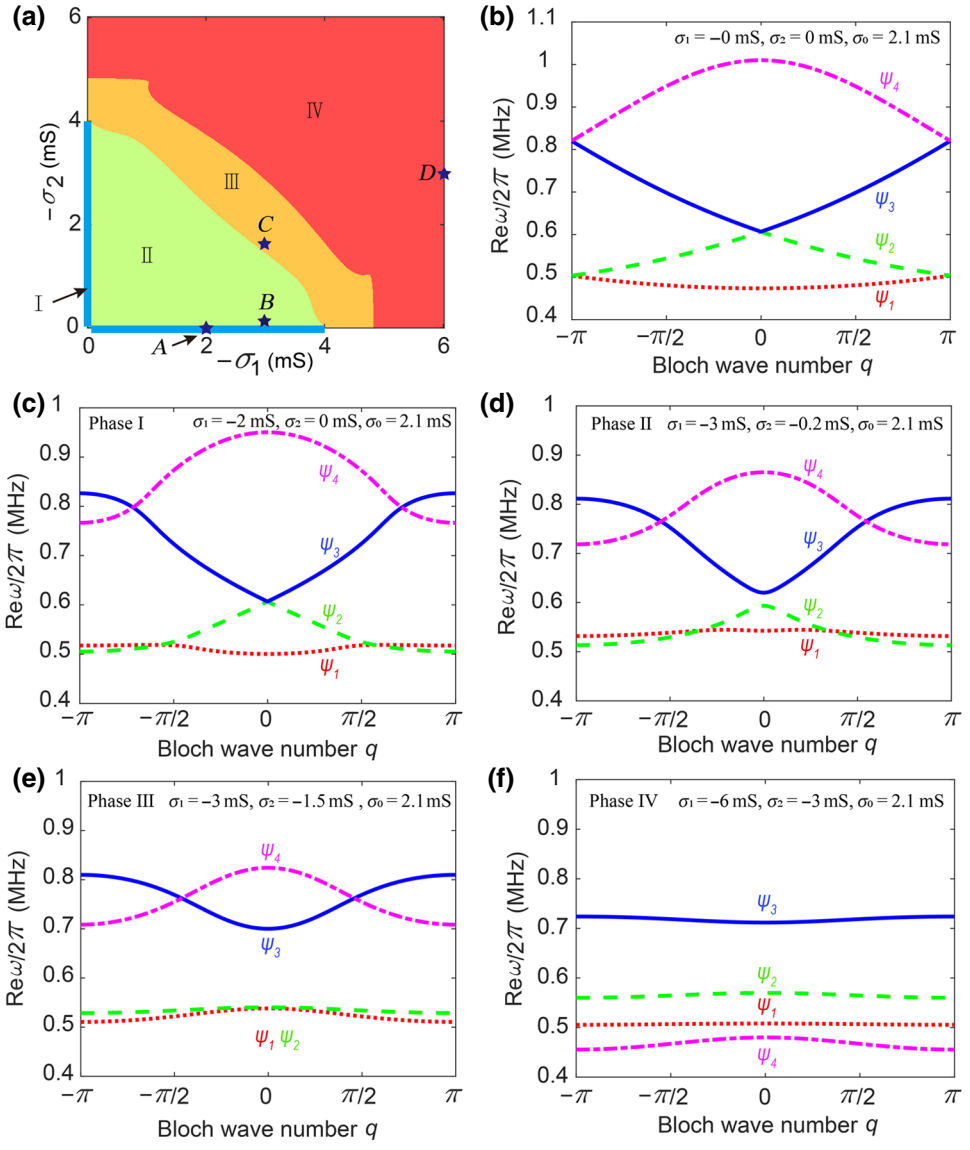

FIG. 2. Phase diagram and band structures of the four phases for the bulk circuit model. (a) Numerically obtained phase diagram of the bulk circuit model with global-loss offset of $\sigma_0 = 2.1$ mS, which is divided into four different phase regions in the σ_1-σ_2 plane, ranging from 0 to -6 mS. Blue lines located on the x and y axes represent phase I. (b) Bulk band structure, Re$\omega(q)$ with $\sigma_1 = 0$, $\sigma_2 = 0$, $\sigma_0 = 2.1$ mS. (c) Re$\omega(q)$ with $\sigma_1 = -2$ mS, $\sigma_2 = 0$ mS, $\sigma_0 = 2.1$ mS, phase I. (d) Re$\omega(q)$ with $\sigma_1 = -3$ mS, $\sigma_2 = -0.2$ mS, $\sigma_0 = 2.1$ mS, phase II. (e) Re$\omega(q)$ with $\sigma_1 = -3$ mS, $\sigma_2 = -1.5$ mS, $\sigma_0 = 2.1$ mS, phase III. (f) Re$\omega(q)$ with $\sigma_1 = -6$ mS, $\sigma_2 = -3$ mS, $\sigma_0 = 2.1$ mS, phase IV.

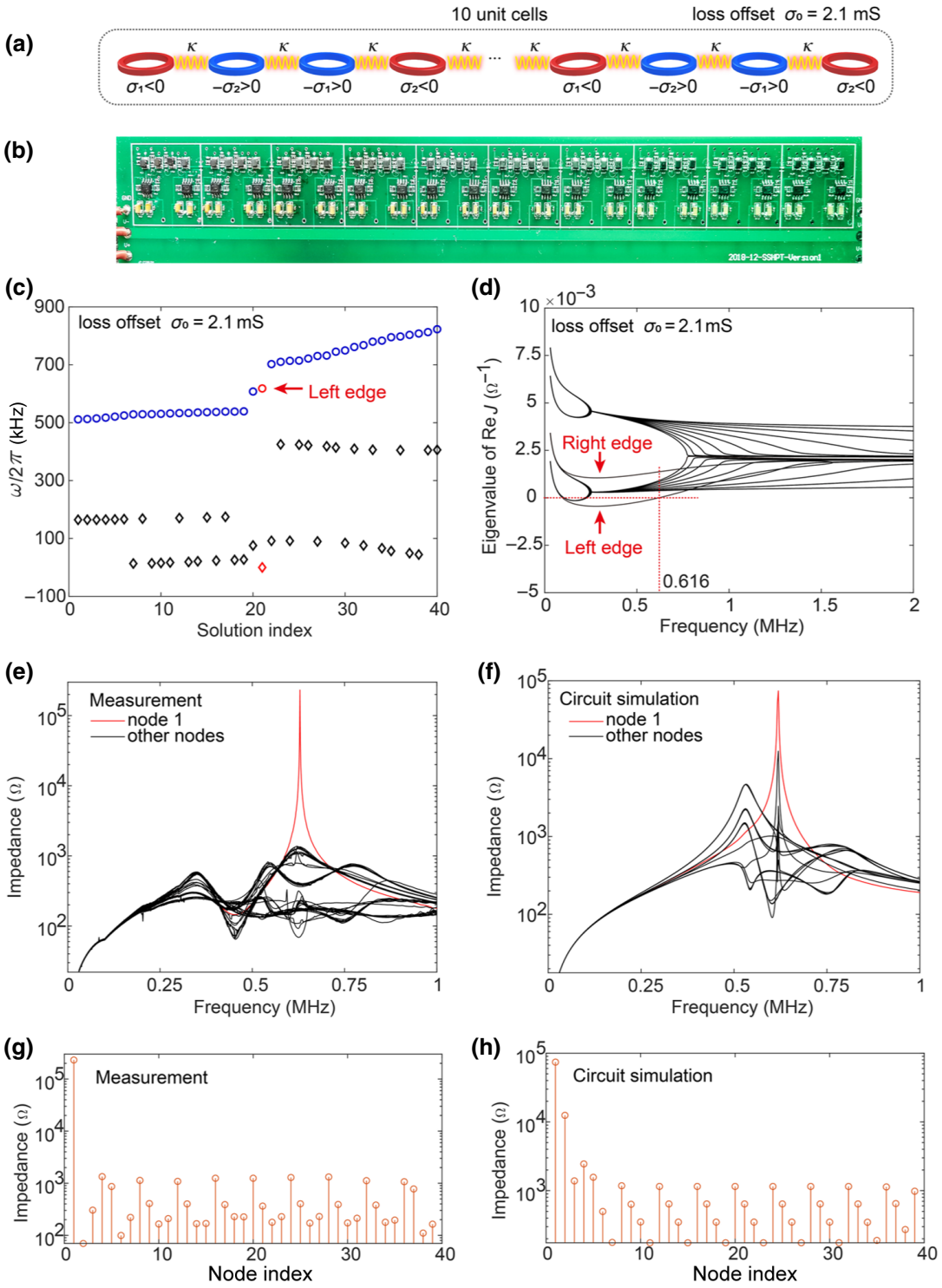

FIG. 3. Experimental and theoretical results for the left edge mode. (a) Schematic illustration of the finite circuit chain containing 10 unit cells, with $\sigma_1 = -3$ mS, $\sigma_2 = -1.5$ mS, and $\sigma_0 = 2.1$ mS. (b) Fabricated sample. (c) Sorted eigenfrequencies of the finite circuit chain. The imaginary part of the left edge mode (red) is shifted to zero through the global-loss offset, $\sigma_0 = 2.1$ mS. Circles and diamond markers represent the real and imaginary parts of the eigenfrequencies, respectively. (d) Real part of the eigenvalue spectra of $J(\omega)$ for the finite circuit chain. The two isolated curves represent the two edge modes. The global-loss offset, $\sigma_0 = 2.1$ mS, shifts the lower isolated curve to zero admittance at the midgap frequency (616 kHz). (e),(f) Experimentally measured and simulated (frequency domain solver) impedance spectra of the finite circuit chain, respectively. Red curve indicates the impedance measured across the leftmost coupling capacitors. (g),(h) Experimentally measured and simulated (frequency domain solver) impedance distributions of the finite circuit chain, respectively.

601×601 data points in the σ_1-σ_2 plane ranging from 0 to -6 mS. The band structure can be divided into four regions in the σ_1-σ_2 plane, labeled as I, II, III, and IV, based on whether there are crossings between the upper two bands, between the lower two bands, and the degeneracy at zero momentum ($q = 0$) between the second and third bands, respectively. Notably, phase I is located on the x and y axes from 0 to -4 mS, as indicated by the light blue line in Fig. 2(a). When all resonators have identical loss, that is, with only a nonzero global loss of $\sigma_0 = 2.1$ mS, while $\sigma_1 = 0$, $\sigma_2 = 0$, no band gap is found either in the real part [Fig. 2(b)] or the imaginary part (see Fig. S1a within the Supplemental Material [35]) of the band structure, with the second and third bands touching at $\omega_0 = 620$ kHz, forming a Dirac-like dispersion due to band folding at $q = 0$.

Interesting physics emerge as we add distributed gain and loss to the circuit, that is, when $\sigma_1\sigma_2 \neq 0$. Here, we investigate the band structure of the proposed non-Hermitian circuit for the four points in Fig. 2(a) located in the four different phase regions. Due to the presence of nonzero global loss σ_0, all four bands for any points in the four regions remain complex in the entire first Brillouin zone (BZ; see Fig. S2 within the Supplemental Material [35] for the imaginary part). For point A with $\sigma_1 = -3$ mS, $\sigma_2 = 0$ located in phase I, the degeneracy between the middle two bands at $q = 0$ [Fig. 2(c)] persists, as long as one of $|\sigma_1|$ and $|\sigma_2|$ is zero and the other one remains below 4 mS. There are two linear crossings between the real parts of the two upper bands (ψ_3 and ψ_4) and between that of the two lower bands (ψ_1 and ψ_2). By setting $\sigma_1 = -3$ mS, $\sigma_2 = -0.2$ mS, the circuit enters phase II, as manifested by a lifting of the degeneracy between the middle two bands at zero momentum, $q = 0$ [Fig. 2(d)]. The crossings of the upper two bands and lower two bands still exist at phase II, but they shift towards smaller momentum, q, due to the increased gain and loss profiles. As we further decrease σ_2 to -1.5 mS, the system enters phase III, as identified by the vanishing of the crossings in the real part of lower two bands (ψ_1 and ψ_2) in the first BZ [Fig. 2(e)]. Finally, by setting $\sigma_1 = -6$ mS, $\sigma_2 = -3$ mS, the system enters phase IV, showing four completely separated bands in the entire BZ [Fig. 2(f)]. Details of the band structures with zero global offset and their mode pattern analysis, as well as more phase regions of the circuit, are given in Note S1 within the Supplemental Material [35]. Since the circuit Laplacian at the resonant frequency $\omega_0 = 1/\sqrt{3C_0L_0}$ takes the same form as that of the Hamiltonian of the quantum system in Ref. [29], the eigenvalue of the circuit Laplacian in the momentum space resembles the band structure of the corresponding quantum model, as detailed in Fig. S6 within the Supplemental Material [35]. The 2.1 mS shift observed in the real part of admittance is due to the global-loss offset.

IV. NONTRIVIAL BOUNDARY STATE AT THE CHAIN EDGE

The nontrivial topological feature of the 1D non-Hermitian topological insulator is manifested by its distinct edge state, which appears at the boundaries of a finite chain. However, it should be noted that the observables of topological circuits are different from those in the quantum and photonics systems. Topological circuits are commonly studied through a two-point impedance measured between two adjacent nodes, a and b, subject to an external current excitation, I_0, flowing through them [11–13], which is expressed as

$$Z_{ab}(\omega) = \frac{V_a - V_b}{I_0} = \sum_n \frac{|\psi_{n,a} - \psi_{n,b}|^2}{j_n(\omega)}, \tag{5}$$

in which $\psi_{n,i}$ ($i = a$ or b) and $j_n(\omega)$ are the eigenstates and eigenvalues of $J(\omega)$, respectively. As the roots of $j_n(\omega)$ correspond to the eigenfrequencies of the circuit, $Z_{ab}(\omega)$ diverges, when the denominator $j_n(\omega)$ crosses zero. Hence, every pole in $Z_{ab}(\omega)$ represents a mode (either bulk or edge) in the finite circuit. Hence, an edge state could be identified at the circuit boundary by a strong resonant peak in the impedance spectra at ω_0.

To demonstrate the existence of the topological edge state in our non-Hermitian circuit, a circuit chain with 10 unit cells, as illustrated in Fig. 3(a), is fabricated using PCB technology [Fig. 3(b)]. A vector network analyzer (Agilent 8753ES) operating from 30 kHz to 6 GHz is used to measure the impedance spectra between each adjacent resonator. To provide an appropriate frequency range for the OA and to obtain a distinct impedance peak in the measurement, the values of the inductors and capacitors are chosen to be $L = 470$ μF and $C = 470$ pF, respectively. To be consistent with experiments, in the theoretical calculations, we consider a Q factor of about 40 for the inductors by adding an imaginary part to the inverse inductance matrix, **W**.

In the experiment, a high-speed low-distortion voltage feedback amplifier (Texas Instrument, LM6171) is used to construct the negative resistor module, which generates the same amount of energy ($P = VI$) as that consumed by a positive resistor. The negative resistor is experimentally tested to have a small deviation of the nominal resistance (4%), which falls in the typical tolerance range of a commercial resistor. Wire wound inductors with (Murata, 2% tolerance) a Q factor of over 40 (at 600 kHz) and 4 Ω dc resistance are chosen to help achieve a high-precision circuit response and sharp impedance resonance. A 4 Ω dc resistance is set for the inductors. In the measurement, a dc power supply (Agilent E3648A), with two independent channels, provides ±15 V dc voltage for the OA. The 2.2 μF and 2 pF capacitors are connected in parallel with the dc supply pin of the OA to minimize the ripple current. A vector network analyzer (Agilent 8753ES),

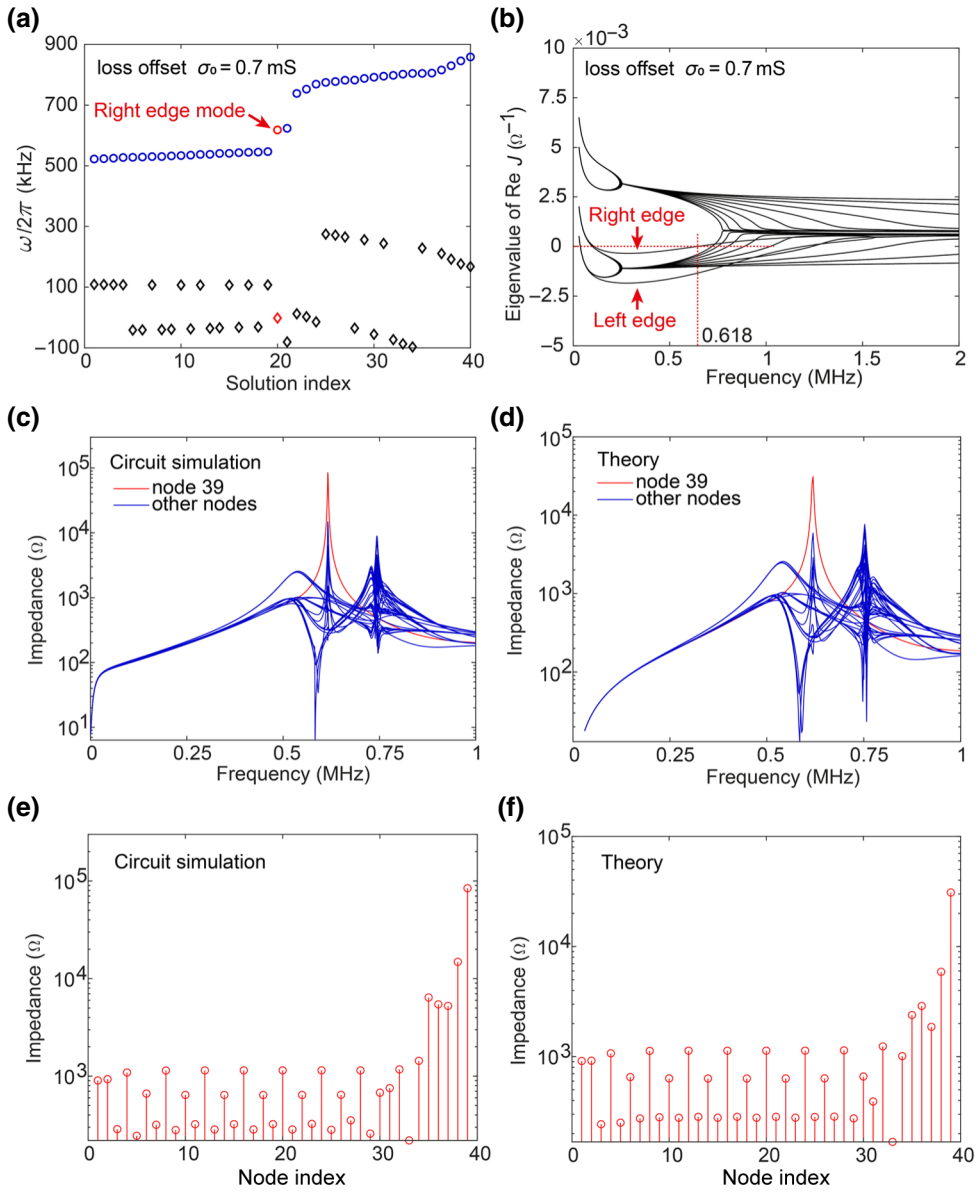

FIG. 4. Numerical and theoretically calculated results for the right edge mode. (a) Sorted eigenfrequencies of the finite circuit chain. The imaginary part of the left edge mode (red) is shifted to zero through the global-loss offset, $\sigma_0 = 0.7$ mS. (b) Real part of the eigenvalue spectra of $J(\omega)$ for the finite circuit chain. The upper isolated curve representing the left edge mode crosses zero at 618 kHz. (c),(d) Numerically simulated (frequency domain solver) and theoretically calculated impedance spectra of the finite circuit chain, respectively. Red curve indicates the impedance measured across the leftmost coupling capacitors. (e),(f) Numerically simulated (frequency domain solver) and theoretically calculated impedance distributions of the finite circuit chain, respectively.

working from 30 kHz to 6 GHz, is used to measure the impedance spectra between each adjacent resonator. As the OA is a nonlinear circuit element, its operational status is highly dependent on the input power. In the experiment, the input power is finely adjusted to 8.61 dBm to achieve a maximum resonant impedance at the edge-state eigenfrequency 612 kHz. In the numerical simulation, we employ the realistic PSpice model for the OA (LM6171 PSPICE Model) provided by Texas Instruments.

Initially, we set the system to phase III by letting $\sigma_1 = -3$ mS and $\sigma_2 = -1.5$ mS, which corresponds to resistances of $R_1 = 330\ \Omega$ and $R_2 = 680\ \Omega$ in Fig. 1(b). Figure 3(c) shows the real part (blue circle) and imaginary part (black diamond) of the calculated eigenfrequencies of the finite circuit chain. A pair of midgap eigenmodes appear at around 616 kHz, corresponding to two localized edge states at the left and right ends of the circuit chain. The two edge modes are also indicated by two isolated

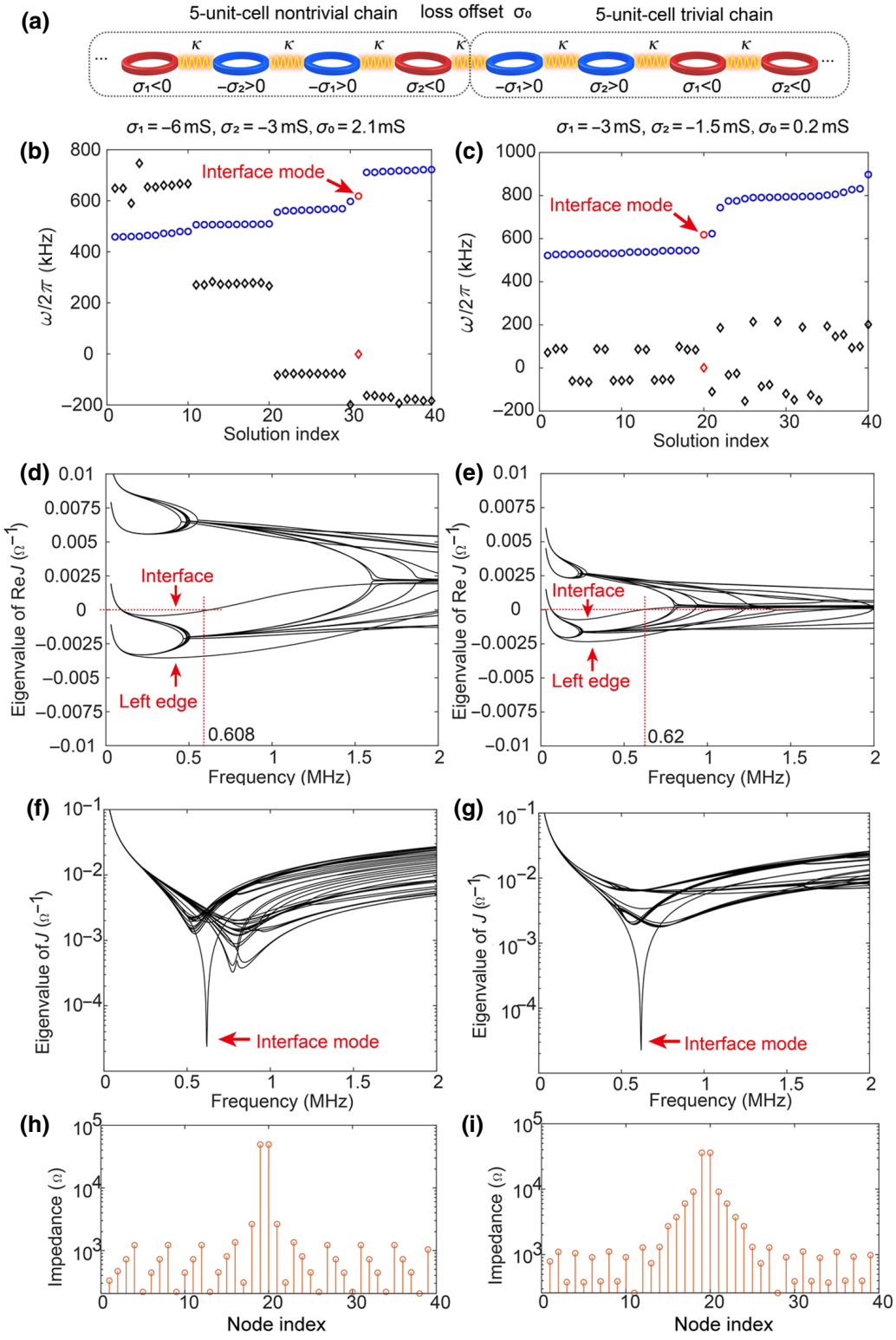

FIG. 5. Demonstration of topological interface mode concentrated at the interface between trivial and nontrivial circuit chains. (a) Schematic illustration of the finite circuit chain with a five-unit-cell nontrivial circuit chain and a five-unit-cell trivial circuit. The trivial circuit is realized by inverting the sign of σ_1. (b),(d),(f) Sorted eigenfrequencies, real part of the eigenvalue of circuit Laplacian $\mathbf{J}(\omega)$, and magnitude of the eigenvalue of circuit Laplacian $\mathbf{J}(\omega)$, respectively, for the first case with $\sigma_1 = -6$ mS, $\sigma_2 = -3$ mS, and $\sigma_0 = 2.1$ mS. (c),(e),(g) Sorted eigenfrequencies, real part of the eigenvalue of circuit Laplacian $\mathbf{J}(\omega)$, and magnitude of the eigenvalue of circuit Laplacian $\mathbf{J}(\omega)$, respectively, for the second case with $\sigma_1 = -3$ mS, $\sigma_2 = -1.5$ mS, and $\sigma_0 = 0.2$ mS. (h),(i) Theoretically calculated impedance distributions for the first and second cases, respectively.

curves in the real part of the eigenvalues of the finite circuit Laplacian, as shown in Fig. 3(d). Since the eigenvalue of j_n for the left edge mode crosses zero at around 616 kHz (see Fig. S8a within the Supplemental Material [35]), one expects a strong localization of the impedance at the left edge. Figures 3(e) and 3(f) show the measured and simulated spectra of impedance measured between all adjacent nodes, respectively, and they match reasonably well with each other. The impedance spectrum between the two leftmost nodes (red curve) shows a distinct peak over 10^5 Ω at 616 kHz, while the impedances measured between all other adjacent nodes (black curves) are much lower. The slight discrepancy between the measurement and simulation is mostly due to the nonideal operating status of the OA in the real circuit network, which is difficult to precisely predict in numerical simulations using PSpice model (see Sec. IV). To directly observe the localization effect of the nontrivial edge state, in Figs. 3(g) and 3(h) we present the measured and simulated impedance distributions at the edge-mode frequency, respectively. The presence of a nontrivial edge state is indicated by a prominent impedance peak localized at the left edge.

To excite the right edge mode, one needs to change the global-loss offset to $\sigma_0 = 0.7$ mS based on our calculation. Figure 4(a) shows the calculated eigenfrequencies for the same finite circuit chain with a global-loss offset of $\sigma_0 = 0.7$ mS. In this case, the imaginary part of the right edge mode is shifted to zero at 618 kHz [Fig. 4(a)], as shown by Fig. 4(b), due to a vanishing eigenvalue j_n (see Fig. S8b within the Supplemental Material [35]). Figure S8c within the Supplemental Material [35] shows the simulated impedance spectra between all adjacent nodes. As expected, we observe an impedance peak of about 10^5 Ω between the two rightmost nodes at the edge frequency of 618 kHz, as highlighted by the red curve, which agrees well with the theoretical results calculated from the circuit Laplacian [Fig. 4(d)]. The numerically (frequency domain solver) and theoretically calculated impedance distributions shown in Figs. 4(e) and 4(f), respectively, further reveal the tight localization of the impedance at the right edge.

However, for the right edge mode with a smaller $\sigma_0 = 0.7$ mS, the edge mode and some of the bulk modes are in lasing mode, as observed from the sorted eigenfrequencies in Fig. 4(a). Such modes with negative imaginary parts are unstable in our circuit because the OA cannot supply continuously increasing power, and thus, does not produce the desired circuit responses, as shown in Fig. 4(f), simulated with the frequency domain solver. Hence, the right edge mode is considered to be nonphysical. While such an issue does not occur in the case of the left edge mode, as the imaginary parts of all modes are negative [Fig. 3(c)] due to the larger global-loss offset ($\sigma_0 = 2.1$ mS).

V. NONTRIVIAL INTERFACE STATE BETWEEN TRIVIAL AND NONTRIVIAL CHAINS

Similar to the SSH model in condensed matter physics, the nontrivial edge state exists not only at the edge of a nontrivial lattice, but also at the interface between nontrivial and trivial circuit chains, as illustrated in Fig. 5(a), where both chains contain five unit cells. The trivial circuit chain is realized by inverting the sign of σ_1. In the first case, the left chain is set in phase IV with $\sigma_1 = -6$ mS, $\sigma_2 = -3$ mS. A pair of midgap modes appear at around 608 kHz [Fig. 5(b)], in which the left and right modes correspond to the edge mode at the left boundary and the interface mode at the center of the chain, respectively. To observe the interface state, we offset the imaginary part of the right edge mode to zero by adding a global-loss offset, $\sigma_0 = 2.1$ mS. Now the upper isolated eigenvalue curve in Fig. 5(d) crosses zero at the interface mode frequency, 608 kHz, which can also be confirmed from the magnitude of $j_n(\omega)$ in Fig. 5(f). We observe a distinct impedance peak at the center of circuit, which decays exponentially into the bulk [Fig. 5(h)].

In the second case, the left chain is set in phase III with $\sigma_1 = -3$ mS, $\sigma_2 = -1.5$ mS. Similar to the first case, a pair of interface modes emerge between the gap of the bulk modes at around 620 kHz [Fig. 5(c)]. In this case, the left one corresponds to the interface mode, which is shifted to a purely real eigenfrequency via the global-loss offset, $\sigma_0 = 0.2$ mS. This is confirmed in Fig. 5(e), in which the upper one is shifted to zero admittance at the interface mode frequency, resulting in a vanishing eigenvalue, j_n, in the magnitude of $j_n(\omega)$ [Fig. 5(g)]. We observe from Fig. 5(i) that the impedance peak which identifies the interface state exhibits a slower decaying rate than that in the first case. This is due to the appearance of bulk modes near the interface mode frequency, as observed from the real part of $j_n(\omega)$ in Fig. 5(e). As a consequence, the slope of the localized impedance peak in the impedance distribution plot [Fig. 5(i)] is not as steep as that in the first case. Notably, these two cases are not physically realizable because some of the bulk modes are in the lasing mode.

VI. CONCLUSION

We propose and experimentally demonstrate a 1D non-Hermitian topological circuit in electrical circuits that exhibits highly pronounced impedance resonance at the boundary of the nontrivial lattice. The topological phase is highly robust against local disorder of the circuit components of 5%–20% tolerances (see Note S3 with in the Supplemental Material [35]). Importantly, one can conveniently introduce nonlinear effects into the non-Hermitian topological circuit by employing nonlinear circuit elements, for instance, varactor diodes [18,36], transistors,

and operational amplifiers. Topological circuits are currently providing us with a convenient experimental platform for exploring new topological physics in the classical regime. Our work may pave the way for tunable topological circuits by properly utilizing active components, such as photoresistors, the resistance of which is controlled by the light intensity. The wide range of circuit functions of OA (including addition, subtraction, integration, and differential, etc.) also provide highly flexible configurations for the design of hopping parameters, promising interesting designs with unusual topological properties.

ACKNOWLEDGMENTS

This work is funded by the European Union's Horizon 2020 Research and Innovation Programme under Marie Skłodowska-Curie Grant No. 833797, the Wolfson Foundation, Horizon 2020 Action Project No. 734578 (D-SPA), the National Key Research and Development Program of China (Grant No. 2017YFA0700201), in part by the National Natural Science Foundation of China (Grants No. 61631007, No. 61571117, No. 61875133, and No. 11874269), the 111 Project (Grant No. 111-2-05), and in part by the China Postdoctoral Science Foundation (Grant No. 2018M633129).

S.L., S.J.M., and C.Y. contributed equally to this work. S.L., S.J.M., and W.L.G. carried out the analytical modeling, numerical simulations. S.L., C.Y., and L.Z. completed the sample fabrication and circuit measurements. As the principal investigators of the projects, S.Z., T.J.C., and Y.J.X. conceived the idea, suggested the designs, planned, coordinated, and supervised the work. S.L., S.J.M., and S.Z. contributed to the writing of the manuscript. All authors discussed the theoretical and numerical aspects and interpreted the results.

[1] G. Harari, M. A. Bandres, Y. Lumer, M. C. Rechtsman, Y. D. Chong, M. Khajavikhan, D. N. Christodoulides, and M. Segev, Topological insulator laser: Theory, Science **359**, eear4003 (2018).

[2] M. A. Bandres, S. Wittek, G. Harari, M. Parto, J. Ren, M. Segev, D. N. Christodoulides, and M. Khajavikhan, Topological insulator laser: Experiments, Science **359**, eear4005 (2018).

[3] V. Peano, C. Brendel, M. Schmidt, and F. Marquardt, Topological phases of sound and light, Phys. Rev. X **5**, 031011 (2015).

[4] Z. J. Yang, F. Gao, X. Shi, X. Lin, Z. Gao, Y. Chong, and B. Zhang, Topological Acoustics, Phys. Rev. Lett. **114**, 114301 (2015).

[5] S. D. Huber, Topological mechanics, Nat. Phys. **12**, 621 (2016).

[6] R. Susstrunk and S. D. Huber, Classification of topological phonons in linear mechanical metamaterials, Proc. Natl Acad. Sci. USA **113**, E4767 (2016).

[7] N. Jia, C. Owens, A. Sommer, D. Schuster, and J. Simon, Time- and site-resolved dynamics in a topological circuit, Phys. Rev. X **5**, 021031 (2015).

[8] V. Albert, L. I. Glazman, and L. Jiang, Topological Properties of Linear Circuit Lattices, Phys. Rev. Lett. **114**, 173902 (2015).

[9] E. Zhao, Topological circuits of inductors and capacitors, Annals Phys. **399**, 289 (2018).

[10] T. Goren, K. Plekhanov, F. Appas, and K. L. Hur, Topological Zak phase in strongly coupled LC circuits, Phys. Rev. B **97**, 041106 (2018).

[11] S. Liu, W. Gao, Q. Zhang, S. Ma, L. Zhang, C. Liu, Y. J. Xiang, T. J. Cui, and S. Zhang, Topologically protected edge state in two-dimensional Su–schrieffer–heeger circuit, Research **2019**, 8609875 (2019).

[12] K. Luo, R. Yu, and H. Weng, Topological nodal states in circuit lattice, Research **2018**, 6793752 (2018).

[13] C. H. Lee, S. Imhof, C. Berger, F. Bayer, J. Brehm, L. W. Molenkamp, T. Kiessling, and R. Thomale, Topolectrical circuits, Commun. Phys. **1**, 39 (2018).

[14] Y. Lu, N. Jia, L. Su, C. Owens, G. Juzeliunas, D. I. Schuster, and J. Simon, Probing the berry curvature and Fermi arcs of a weyl circuit, Phys. Rev. B **99**, 020302 (2019).

[15] S. Imhof, C. Berger, F. Bayer, J. Brehm, L. W. Molenkamp, T. Kiessling, F. Schindler, C. H. Lee, M. Greiter, T. Neupert, and R. Thomale, Topolectrical-circuit realization of topological corner modes, Nat. Phys. **14**, 925 (2018).

[16] M. Ezawa, Higher-order topological electric circuits and topological corner resonance on the breathing Kagome and pyrochlore lattices, Phys. Rev. B **98**, 201402 (2018).

[17] M. Ezawa, Electric-circuit realization of non-Hermitian higher-order topological systems, arXiv:1810.04527 (2018).

[18] Y. Hadad, J. C. Soric, A. B. Khanikaev, and A. Alu, Self-induced topological protection in nonlinear circuit arrays, Nat. Electronics **1**, 178 (2018).

[19] T. Hofmann, T. Helbig, C. H. Lee, and R. Thomale, Chiral voltage propagation in a self-calibrated topolectrical Chern circuit, arXiv:1809.08687 (2018).

[20] K. Luo, J. Feng, Y. X. Zhao, and R. Yu, Nodal Manifolds Bounded by Exceptional Points on Non-Hermitian Honeycomb Lattices and Electrical-Circuit Realizations, arXiv:1810.09231 (2018)

[21] C. M. Bender and S. Boettcher, Real Spectra in non-Hermitian Hamiltonians Having PT Symmetry, Phys. Rev. Lett. **80**, 5243 (1998).

[22] C. E. Ruter, K. G. Makris, R. El-Ganainy, D. N. Christodoulides, M. Segev, and D. Kip, Observation of parity–time symmetry in optics, Nat. Phys. **6**, 192 (2010).

[23] A. Regensburger, C. Bersch, M.-A. Miri, G. Onishchukov, D. N. Christodoulides, and U. Peschel, Parity–time synthetic photonic lattices, Nature **488**, 167 (2012).

[24] R. EI-Ganainy, K. G. Makris, M. Khajavikhan, Z. H. Musslimani, S. Rotter, and N. Christodoulides, Non-Hermitian physics and PT symmetry, Nat. Phys. **14**, 11 (2018).

[25] S. Weimann, M. Kremer, Y. Plotnik, Y. Lumer, S. Nolte, K. G. Makris, M. Segev, M. C. Rechtsman, and A. Szameit, Topologically protected bound states in photonic parity–time-symmetric crystals, Nat. Mater. **16**, 433 (2017).

[26] C. Poli, M. Bellec, U. Kuhl, F. Mortessagne, and H. Schomerus, Selective enhancement of topologically

induced interface states in a dielectric resonator chain, Nat. Commun. **6**, 6710 (2015).

[27] H. Menke and M. M. Hirschmann, Topological quantum wires with balanced gain and loss, Phys. Rev. B **95**, 174506 (2017).

[28] B. Zhu, R. Lu, and S. Chen, PT symmetry in the non-hermitian Su-schrieffer-heeger model with complex boundary potentials, Phys. Rev. A **89**, 062102 (2014).

[29] K. Takata and M. Notomi, Topological Insulating Phase Induced Solely by Gain and Loss, Phys. Rev. Lett. **121**, 213902 (2018).

[30] S. Ryu, A. Schnyder, A. Furusaki, and A. Ludwig, Topological insulators and superconductors: Tenfold way and dimensional hierarchy, New J. Phys. **12**, 065010 (2010).

[31] M. Sato, K. Hasebe, K. Esaki, and M. Kohmoto, Time-reversal symmetry in non-Hermitian systems, Prog. Theor. Phys. **127**, 937 (2012).

[32] K. Esaki, M. Sato, K. Hasebe, and M. Kohmoto, Edge states and topological phases in non-Hermitian systems, Phys. Rev. B **84**, 205128 (2011).

[33] S.-D. Liang and G.-Y. Huang. Topological invariance and global Berry phase in non-Hermitian systems, Phys. Rev. A **87**, 012118 (2013).

[34] T. E. Lee, Reply to comment on "Anomalous Edge State in a Non-Hermitian Lattice," arXiv:1611.00355.

[35] See the Supplemental Material at http://link.aps.org/supplemental/10.1103/PhysRevApplied.13.014047 for more discussion on the bulk band properties with zero global loss, derivation of the circuit Hamiltonian, and topological robustness.

[36] Y. Wang, L. Lang, C. H. Lee, B. Zhang, Y. D. Chong, Topologically Enhanced Harmonic Generation in a Nonlinear Transmission Line, arXiv:1807.11163 (2019)